RESEARCH PAPER

Increasing flow rates in polydimethylsiloxane-based deterministic lateral displacement devices for sub-micrometer particle separation

Julius Marhenke[1] · Tobias Dirnecker[1] · Nicolas Vogel[2] · Mathias Rommel[3]

Abstract

In this study, we show the design and manufacturing of microfluidic deterministic lateral displacement (DLD) devices for sub-micrometer particle separation. For that purpose, devices with pillar gaps of 4 μm and a periodicity of 50 were designed. After photolithographic manufacturing of SU-8 masters with different heights (15 and 30 μm) and vertical sidewalls for soft-lithographic replication with polydimethylsiloxane (PDMS) the influence of flow rate on the separation efficiency of 0.45 and 0.97 μm particles was investigated. The 15 μm devices were operated at 0.125 and 0.5 μl/min sample flow rate and the 30 μm devices at 0.5 and 2.0 μl/min, respectively. Excellent separation efficiencies were observed for both device heights at the lower sample flow rates, while separation efficiencies decreased at the respective higher sample flow rates. The decrease in separation efficiency was attributed to deformation of the soft PDMS pillars, which causes an increase in pillar gaps at the higher sample flow rates as shown by microscopy imaging. The advantage of the 30 μm devices over the 15 μm devices is clearly shown by the separation of 0.45 and 0.97 μm particles at 0.5 μl/min. Due to reduced hydrodynamic resistance in the 30 μm devices and thus less pillar deformation, the displacement efficiency of 0.97 μm particles was above 99% compared to 46–57% for the 15 μm devices. Our 30 μm devices demonstrated excellent separation at a tenfold higher sample flow rate with 0.5 μl/min compared to comparable PDMS-based devices operating in the same size regime.

Keywords Deterministic lateral displacement (DLD) · Polydimethylsiloxane (PDMS) · Flow rate · Deformation

1 Introduction

Microfluidic devices are miniaturized setups to control the flow of liquids or dispersions with high precision and minimal sample volumes under continuous flow (Whitesides 2006). As such, they are useful tools to study and control chemical reactions (Kessler et al. 2020; Shastri et al. 2015), create emulsions, double emulsions and solid particles with very high precision (Abate and Weitz 2009; Amstad 2017; Datta et al. 2014; Perrotton et al. 2019), or study self-assembly phenomena (Vogel et al. 2015; Wang et al. 2018). One of the most important areas of application is in the biomedical field (Azizipour et al. 2020; Sia and Whitesides 2003; Velve-Casquillas et al. 2010). Benefits of microfluidic devices include the potential to mimic biological conditions (Azizipour et al. 2020; Velve-Casquillas et al. 2010) leading to more realistic experimental conditions, enormous integration possibilities for Lab-on-a-Chip (Azizipour et al. 2020; Gupta et al. 2016) and Organ-on-a-Chip (Azizipour et al. 2020; Boyang Zhang et al. 2018) devices, as well as the opportunity to exploit properties that are only or more easily accessible at the microscale (Boyang Zhang et al. 2018). A laminar flow profile is an important example of such a property, which is often encountered in microfluidic devices (Azizipour et al. 2020; Sia and Whitesides 2003; Velve-Casquillas et al. 2010). This laminar flow profile provides highly regular conditions that can be exploited in sophisticated applications of microfluidic devices. In particular, deterministic lateral displacement (DLD) devices exploit this regular laminar flow for particle separation based on their hydrodynamic diameter.

✉ Julius Marhenke
  julius.marhenke@fau.de

[1] Friedrich-Alexander-Universität Erlangen-Nürnberg, Electron Devices, Cauerstraße 6, 91058 Erlangen, Germany

[2] Friedrich-Alexander-Universität Erlangen-Nürnberg, Institute of Particle Technology, Cauerstraße 4, 91058 Erlangen, Germany

[3] Fraunhofer Institute for Integrated Systems and Device Technology IISB, Schottkystraße 10, 91058 Erlangen, Germany

The working principle of DLD was first described by Huang et al. in 2004 (Huang et al. 2004). In a DLD device, particles are separated by a flow profile that results from a precisely arranged pillar array. The separation arises from a lateral displacement of particles above a critical diameter while particles below the critical diameter can traverse the DLD device without lateral displacement (Salafi et al. 2019). This results in a spatial separation of particles based on their diameter.

Since the first description of the DLD principle numerous devices have been designed, simulated and tested in the fields of blood fractionation (Inglis et al. 2008, 2011), circulating tumor cell separation (Jiang et al. 2017; Liu et al. 2013) or filtering satellite droplets of microfluidic droplet generators (Joensson et al. 2011; Tottori et al. 2017; Tottori and Nisisako 2018).

Separation down to 20 nm is possible (Wunsch et al. 2016), but requires expensive, complex and time-consuming fabrication of silicon devices. A widely used and simple alternative are PDMS-based devices, with PDMS being one of the most used materials for microfluidic devices (Raj M and Chakraborty 2020). PDMS offers several attractive properties including biocompatibility, transparency, ease of device manufacturing and the possibility to rapidly replicate microfluidic devices from a master substrate.

However, the soft nature of PDMS poses great challenges to accurately reproduce small feature sizes required for the separation of nanoscale particle systems (Sia and Whitesides 2003; Velve-Casquillas et al. 2010). To date PDMS-based DLD devices capable of sub-micrometer particle separation reported in literature are scarce (Tottori et al. 2020; Zeming et al. 2018) and usually shallow to avoid pillar deformation and bending at smaller pillar gaps with increased height. The reported devices had channel heights of 3 μm (Zeming et al. 2018) and 4 μm (Tottori et al. 2020), respectively. These shallow heights can limit the device's throughput (Hochstetter et al. 2020) as the hydrodynamic resistance scales inversely with the channel height.

This study aims to investigate the separation of sub-micrometer particles at varied flow rates in PDMS-based DLD devices. As the separation of sub-micrometer particles requires small pillar gaps, the hydrodynamic resistance of the resulting DLD device increases (Hochstetter et al. 2020) compared to a device for separation of larger particles. Devices with higher hydrodynamic resistance must be operated with higher pressure to achieve the same flow rate, which can lead to pressure-induced deformation of pillars in PDMS-based devices (Inglis 2010). Therefore, overcoming hydrodynamic resistance is a key challenge to increase flow rates in DLD devices. To investigate the influence of the hydrodynamic resistance for separation of sub-micrometer particles, devices with different heights (15 and 30 μm) and a designed pillar gap of 4 μm were manufactured. The devices

were then run at different flow rates (0.125, 0.5 and 2 μl/min) with mixtures of 0.45 and 0.97 μm fluorescent polystyrene particles. The displacement efficiencies of the devices for the differently sized particles at different operation parameters were determined.

2 Methods and experiments

2.1 Design of DLD devices

First, the design of the DLD device and, in particular, the shape, geometry and fabrication of the pillar array is introduced (Fig. 1).

The inlet region of the DLD devices was designed with three individual ports. The two outer inlet ports were used for a buffer solution, while the centered inlet port was used for the sample particle dispersion. Each buffer port is connected by five channels, and the sample port by one channel to the pillar array, respectively. The width of all inlet channels was 200 μm. However, since the buffer channels consist of five parallel-connected channels, the hydrodynamic resistance is reduced to one-fifth of the sample channel's hydrodynamic resistance. To ensure parallel flow entering the pillar array, all channels should have the same resistance (Davis 2008), thus, the length of the buffer channels is five-times the sample channel length.

All outlet channels were designed with a width of 140 μm. Since the same number of channels was connected in parallel for each outlet port, the length of all outlet channels was the same (Fig. 1). All inlet and outlet channels were separated by 25 μm walls at the closest.

The critical diameter, above which particles are being displaced in the device, is mainly influenced by two geometrical pillar array factors, as proposed by the model of Davis (Davis 2008). The first geometrical pillar array factor is the pillar gap G (Fig. 1a) between two neighboring pillars perpendicular to the fluid flow direction and the second factor is the periodicity (N) of the pillar array. The periodicity results from a shift of the lateral pillar position in each adjacent pillar row perpendicular to the fluid flow direction. Estimation of critical diameters D_c in this work is based on the model by Davis and can be calculated with the following equation (Davis 2008):

$$D_c = 1.4 \, GN^{-0.48} \tag{1}$$

To reduce the critical diameter G can be reduced or N can be increased. Increasing N has the advantage that larger pillar gaps can be designed, which are easier to realize and fabricate accurately by photolithography, especially when further considering increased device heights of 15 and 30 μm. However, Davis recommends, as a rule of thumb,
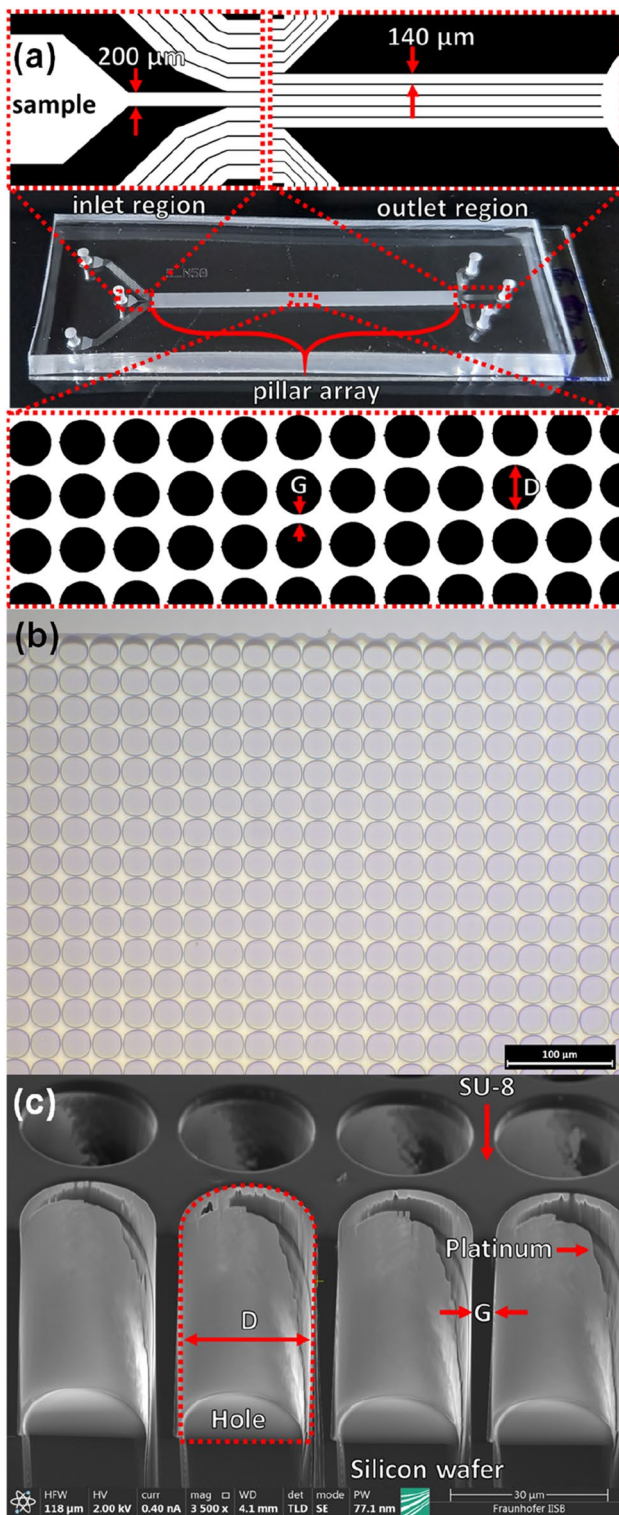
Fig. 1 **a** Exemplary image of a PDMS-based DLD device with schematic magnifications (not to scale) of the inlet and outlet region as well as the pillar array with pillar gap G and pillar diameter D. **b** Microscopy image of a replicated pillar array in PDMS with a pillar gap of 4 μm and periodicity of 50. **c** Focused ion beam cross-section of a SU-8 master on a silicon wafer, manufactured using an i-line filter during exposure. Platinum, deposited for cross-section preparation, and some preparation artefacts are visible

that N should not be greater than 50 (Davis 2008), which was chosen as the periodicity for the DLD devices in this work to maximize the required pillar gap. To achieve a sub-micrometer separation, a pillar gap of 4 μm was designed, leading to a critical diameter of 0.9 μm. The pillar height was chosen to be 15 μm and 30 μm to increase the applicable flow rate compared to typical device designs (Tottori et al. 2020; Zeming et al. 2018), and pillar diameter was designed to be 25 μm to ensure feasible aspect ratios and stable operation conditions. Also, the critical height of lateral collapse (Zhang et al. 2006) for PDMS pillars with the designed dimensions was estimated as shown in the supplementary information. Based on the estimation pillars should start to collapse around 74 μm, so that the designed pillars should be sufficiently stable for manufacturing.

2.2 Manufacturing of DLD devices

The DLD devices were replicated from in-house manufactured master wafers by PDMS molding. Master wafers were manufactured with SU-8 2050 photoresist (MicroChem, U.S.A.) (Fig. 1c) on 150 mm silicon wafers in a clean room. SU-8 was chosen due to the possibility of achieving thick photoresist layers (> 200 μm) in a single spin coating step (Campo and Greiner 2007). The SU-8 was spin coated with 4000 and 6000 rpm for 60 s to produce different layer thicknesses and structured by standard photolithography with a mask aligner MA6 (Süss GmbH, Germany). An i-line filter was used to ensure vertical sidewalls of the SU-8 (Campo and Greiner 2007). After hard baking, the step height was measured with a P-16 + stylus profilometer (KLA-Tencor, U.S.A.) at six different locations spread over the wafer. The measured thicknesses were 30.3 ± 1.5 (30 μm) and 15.4 ± 0.9 μm (15 μm) for 4000 and 6000 rpm, respectively. Therefore, the resulting aspect ratios in our pillar arrays were 1.2:1 and 0.6:1. A focused ion beam (Helios G4 PFIB CXe, ThermoFisher Scientific, U.S.A.) cross section image of the SU-8 master wafer, highlighting the accurate vertical walls, is shown in (Fig. 1c). More information on the processing parameters can be found in the supplementary information. An anti-sticking layer of Trichloro-(1H,1H,2H,2H-perfluorooctyl) silane (Sigma-Aldrich, U.S.A.) was applied to facilitate PDMS separation from the master wafers.

For PDMS molding Sylgard 184 (Dow Corporate, U.S.A.), which consists of a base and curing agent that were mixed in a ratio of 10:1 by weight, was used. After mixing, the PDMS was degassed in a desiccator and then poured onto the master wafers. After curing at 50 °C for at least 20 h, the PDMS was peeled off the wafer and the inlet and outlet holes were structured with a 1.5 mm biopsy punch.

The structured PDMS DLD devices were permanently bonded onto a glass microscope slide. Both the PDMS and glass were treated for 30 s with a mixture of argon

and oxygen plasma. Afterwards the treated surfaces were brought into contact for irreversible bonding and the finished DLD devices could be used.

2.3 Operation of DLD devices

To investigate the performance of the DLD devices, a dispersion of 0.45 ± 0.10 and 0.97 ± 0.03 µm fluorescently labelled polystyrene particles was used (Microparticles GmbH, Germany). Particles were purchased in a concentration of 2.5 wt.-% and 0.5 µl of the 0.45 and 0.75 µl of the 0.97 µm particles were diluted in 5 ml of water. The 0.45 µm particles were labeled with a green pyrromethene fluorescent dye and the 0.97 µm particles were labeled with a red squaraine fluorescent dye. DI water was used as the buffer fluid. To avoid clogging, 1 vol.-% Tween-20 (Sigma-Aldrich, U.S.A.) was added to all used fluids.

Two Fusion 100 Touch syringe pumps (Chemyx, U.S.A.) were used to run the DLD devices. First, the buffer was applied into the DLD devices. After the buffer fluid filled the entire inlet region of the DLD devices, the sample particle dispersion was connected to the DLD devices. The DLD devices were flushed with the particle dispersion prior to inserting pipette tips for sample collection. The flushing and operation of a DLD device is also illustrated in supplementary video 1. An overview of all experimental parameters is given in Table 1. For each set of parameters, two runs were conducted.

The chosen sample flow rates for the 15 µm devices were 0.125 and 0.5 µl/min, while the 30 µm devices were operated with 0.5 and 2.0 µl/min. The reason for not applying the lowest sample flow rate of 0.125 µl/min to the 30 µm device was that the flush time in 15 µm device already had to be doubled and had to be increased further for the 30 µm device due to the greater volume of the devices. On the other hand, an applied sample flow rate of 2.0 µl/min to the 15 µm device led to the tubing being pushed out of the inlets due to the increased pressure.

Table 1 Overview of experimental parameters for particle displacement experiments

Devices	Flow rate in µl/min		Flush time in min	Sample collection time in min
	Sample	Buffer		
15 µm	0.125	0.625	60	120
	0.5	2.5	30	60
30 µm	0.5	2.5	30	60
	2	10	30	60

The applied buffer flow rate at each buffer inlet is always 5 times the sample flow rate as of the design of the DLD devices. The collective buffer flow rate is twice the values in the table as it is applied to both buffer inlets

2.4 Characterization of DLD device separation

The displacement efficiencies of the DLD devices were characterized by confocal fluorescence microscopy (TCS SP5, Leica, Germany). Displacement efficiency in this work is defined as the fraction of particles measured in outlet 1 (collecting displaced particles) divided by the total amount of particles of the same size measured in all three outlets. For a reliable separation, the displacement efficiency of larger particles should be as high as possible while it should be as low as possible for smaller particles.

For particle detection, a 1 µl droplet of the collected sample fluid from the outlets was dried on a cover slip. The entire area covered by the dried particle dispersion was scanned with a fluorescence microscope. The 0.45 ± 0.10 µm particles labeled with green fluorescent dye were excited with a laser emitting at 488 nm and the 0.97 ± 0.03 µm particles labeled with red fluorescent dye were excited with a laser emitting at 633 nm. The emitted light of the particles was collected in the range of 500 to 550 nm for the green fluorescent dye and in the range of 650 to 700 nm for the red fluorescent dye. Images were analyzed with Fiji (Schindelin et al. 2012) (version 1.53c) to determine the total number of particles in the dried droplet. For that purpose, the fluorescent images were converted into binary images and individual particles were counted (details in supplementary information and Fig. S1).

3 Results and discussion

3.1 DLD device structures and separation characteristics

Prior to displacement experiments, the pillar diameter and gap of the molded DLD devices were determined. For that purpose, three microscopy images of molded DLD devices were taken for each height. The pillar diameter was calculated from the pillar area, which was determined by image analysis from the microscopy images. With the designed pillar center to pillar center distance of 29 µm, the pillar gap was then calculated:

$$G = 29 \ \mu m - D. \tag{2}$$

Results and design parameters as well as resulting critical diameters for the devices according to Eq. (1) are shown in Table 2.

The evaluation of the microscopy images showed slightly different pillar diameters and hence also different pillar gaps from the two different master wafers for the different device heights. However, as the pillar gaps of the replicated PDMS

Table 2 Overview of pillar diameter D, gap G and critical diameter D_c for the DLD device design and resulting devices from the produced master wafers of different heights

Devices	DLD parameters in μm		
	D	G	D_c
Design	25	4	0.9
15 μm	26.1 ± 0.2	2.9 ± 0.2	0.62 ± 0.04
30 μm	25.5 ± 0.2	3.5 ± 0.2	0.75 ± 0.04

devices were slightly smaller than expected from the design, the calculated critical diameters for both device heights (Table 2) were shifted to smaller values. To demonstrate the successful separation of sub-micrometer particles, we therefore chose particle populations with sizes that were equally spaced from this critical diameter and used 0.97 μm particles and 0.45 μm particles.

After the theoretical critical diameters were evaluated, the devices were operated with a dispersion containing 0.45 and 0.97 μm particles. As an example, the measured particles for a 30 μm device run at 0.5 μl/min and another one run at 2 μl/min sample flow rate, respectively, are shown in Fig. 2.

At a sample flow rate of 0.5 μl/min, the larger particles ($d = 0.97$ μm) were displaced in outlet 1, while the 0.45 μm particles were found in outlet 2 (Fig. 2a). The displacement efficiency was high ($> 99\%$) for the 0.97 μm particles and low ($< 5\%$) for the 0.45 μm particles, indicating an efficient separation. When the sample flow rate was increased to 2.0 μl/min, the displacement efficiency of the 0.97 μm particles decreased to ~69% (Fig. 2b).

The flow-rate dependent displacement efficiencies of 0.45 and 0.97 μm particles in all devices are summarized in Fig. 3. For the lower flow rates (0.125 μl/min for 15 μm and 0.5 μl/min for 30 μm) an excellent separation of the differently sized particles was achieved, as more than 97% of the 0.97 μm particles and less than 5% of the 0.45 μm particles were displaced. An increase in flow rate by a factor of four, however, decreased the displacement efficiency of the 0.97 μm particles for both device heights to approximately 45–60 and 65–75%, respectively, whereas the displacement efficiencies of the 0.45 μm particles remained below 5%. A reason for the minor effect of increased flowrate on the displacement efficiency for the 0.45 μm particle could be that the displaced 0.45 μm particles are primarily agglomerates, which are already displaced at low flow rates. Increasing the flow rate and thus reducing the critical diameter therefore does not affect their displacement. This is also supported by the average measured size of 13.3 ± 2.2 px^2 compared to 4.6 ± 1.5 px^2 for 0.45 μm particles in outlet 1 compared to outlet 2, respectively.

These findings imply that the separation of the differently sized particles in the centered outlet was reduced, while the
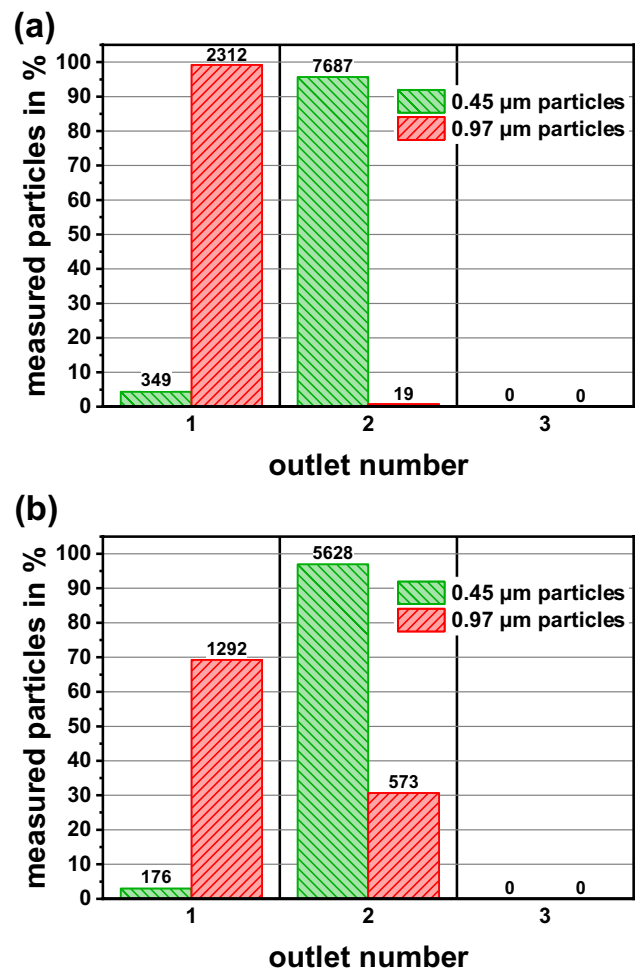

Fig. 2 Measured 0.45 and 0.97 μm particles for all three outlets of the 30 μm devices run at **a** 0.5 and **b** 2.0 μl/min sample flow rate. Numbers above bars indicate the absolute number of particles measured in each outlet

separation of the larger particles into outlet 1 was still high. In absolute numbers, the displacement of 0.97 μm particles per time was even higher compared to the lower flow rate, since the flow rate was increased by a factor of four while the displacement efficiency only reduced to 65–75% for the 30 μm device. For applications requiring only the separation of larger particles, a higher throughput can be achieved by increasing the flow rate.

Another advantage of the higher flow rates was an easier handling of the collected fluids. While microfluidic devices can manage extremely small volumes, it can be difficult to manage those volumes outside of the devices. This was also the reason for the doubled flushing and sample collection time for the 15 μm devices at 0.125 μl/min sample flow rate (Table 1).

Compared to a device by (Tottori et al. 2020), separating 0.5 and 1.0 μm particles, the flow rate in the 30 μm
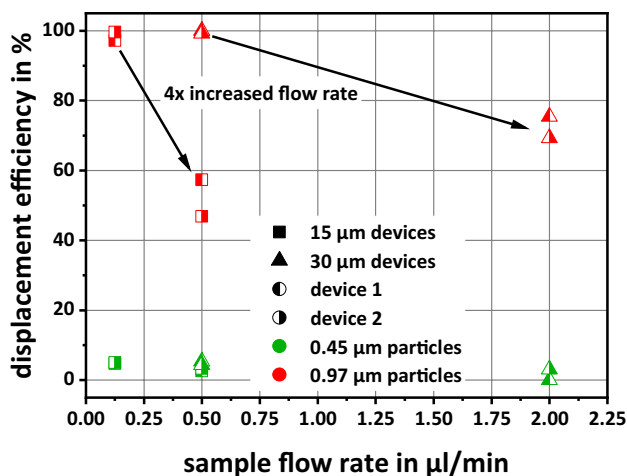
Fig. 3 Displacement efficiency of 0.45 (in green) and 0.97 μm (in red) particles in 15 and 30 μm DLD devices. For each parameter set and both device heights, results of two experiments are shown

device was 10 times higher at 0.5 μl/min. However, the device by Tottori et al. was driven by withdrawal while the devices in this work were run by infusion. While the flow rate of devices operated in withdrawal is directly limited by the device's resistance with a maximum negative pressure difference of 1 bar to atmospheric pressure, the flow rate by infusion operated devices can be higher, since higher pressure differences can be applied. To compare the devices more accurately, the hydrodynamic resistance of the pillar arrays was calculated and compared. According to Davis (Davis 2008) the hydrodynamic resistance of the pillar array (R) can be estimated based on the fluid viscosity (μ), pillar array length (β), width (α), height (H), and pillar gap (G) as follows:

$$R \approx 4.6\left(\mu\beta/\alpha G^2 H\right). \tag{3}$$

An overview of parameters as well as the resulting hydrodynamic resistance of the pillar arrays is given in Table 3. As DLD devices in this work and Tottori's were run with water, a viscosity of 1 mPa•s was used for calculations.

Table 3 Parameters (length (β), width (α), pillar gap (G) and height (H)) of DLD devices used for calculation of the array's hydrodynamic resistance (R)

Device	β in μm	α in μm	G in μm	H in μm	R in mPa · s/μm^3
Tottori et al. 2020	2513	113	2.2	4	5.3
This work	42,054	2440	2.9	15	0.6
			3.5	30	0.2

Based on the calculated resistances the hydrodynamic resistance of the devices in this work was one order of magnitude lower compared to the device by Tottori et al. When applying the same pressure, the flow rate for the devices in this work should be higher. These differences showed that the increased pillar height in our devices allowed a significant increase in flow rate.

3.2 Flow-rate-induced phenomena

To investigate the observed reduction in displacement efficiency at higher flow rates, the DLD devices were run under a microscope to directly observe the response of the device to different flow rates (Fig. 4). Microscopy images were taken at the start of the experiment, after the pillars were wetted, and after the flushing time specified in Table 1 to equilibrate the system at the different flow rates. The images show the beginning of the pillar array near the inlet.

The images show a change of the pillar gap between the lower and higher flow rates, which we attributed to increased pressure. This change in pillar gap was assumed to contribute to the reduction in displacement efficiency, since a bigger pillar gap also shifts the critical diameter upwards. For better visualization of the pillar gap changes by the applied flow rate, overlays of pillars at the different conditions are shown in Fig. 5.

The overlays underline changes in the pillar gaps at the different flow rates. For the pillar gaps after wetting and at the lower flow rate only minor difference could be seen (Fig. 5). However, the overlays of pillars at higher flow rate on wetted pillars clearly showed that the pillars at the higher flow rate were reduced in diameter (Fig. 5) and hence the pillar gap increased. To calculate the change in critical diameter, the difference in pillar dimensions before and after application of flow were quantified by image analysis (Fig. 4, Table 4). Based on the measured changes in pillar gap at the three different operation conditions, the critical diameter for particle separation at those conditions was re-calculated.
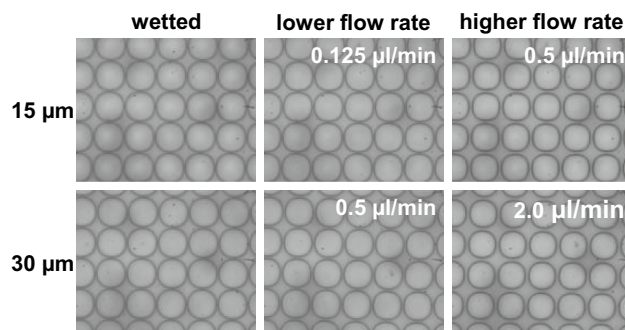

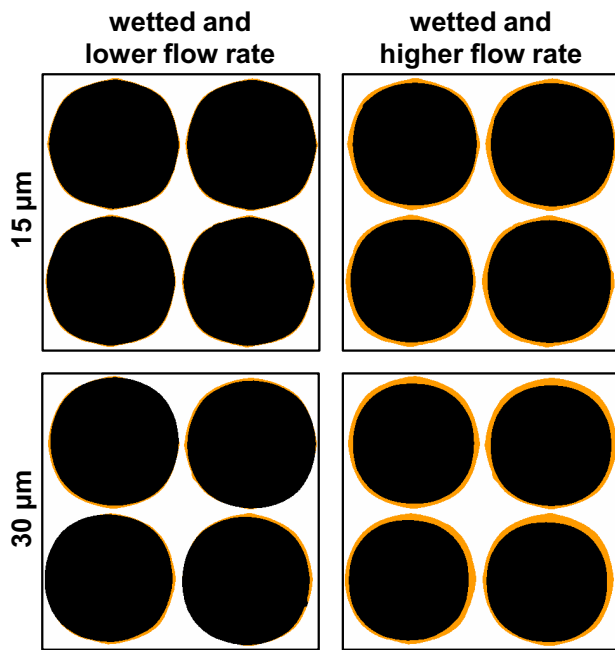**Fig. 4** Microscopy images of pillar arrays from 15 and 30 μm devices ran at lower and higher flow rates

Fig. 5 Overlay of a cropped pillars area from Fig. 4 for 15 and 30 μm devices at different flow rates. Pillar area of wetted pillars is displayed in orange and at lower and higher flow rates in black

As the images showed the pillar gap increased with increasing flow rate. The difference between the just wetted and lower flow rate was minor (Fig. 5). With increasing flow rate, the change in pillar gap became more significant and led to an increase in the calculated critical diameter. For the 15 μm device, the calculated critical diameter increased from 0.6 to 0.9 μm. The critical diameter was thus shifted towards the diameter of the large particles, which caused the reduced displacement efficiency. Note that the critical diameter was calculated for an ideal device based on ideal pillar gap and periodicity. Any defects, inhomogeneities, clogging or particle–fluid and particle–particle interactions could potentially influence the separation characteristics. Furthermore, the channel walls could also influence the separation characteristics (Inglis 2009) as no channel wall correction was designed. However, as shown by Pariset et al. (Pariset et al. 2017) the channel wall influence decreases with the number of pillars in a row perpendicular to the flow direction. As the number of pillars in a row for the used devices was 85 the

channel wall influence should be minor. Also, the particles were not perfectly monodisperse (0.97 ± 0.03 μm). Hence, a reduction in displacement efficiency is reasonable when particle size and calculated critical diameter of a DLD device are close together.

For the 30 μm devices, the change in critical diameter was even more pronounced, as the critical diameter rose from 0.8 to 1.1 μm, even exceeding the size of the 0.97 ± 0.03 μm particles. The remaining displacement of these particles, which was not predicted by the pillar dimensions at high flow rates, may have resulted from the drop of pressure downstream in the device. As the pressure dropped down the device, also the deformation of the pillars was less pronounced (Supplementary Fig. S2) and thus the critical diameter decreased towards the outlet region. At some point in the pillar array, the critical diameter became again smaller than the particle size and the particles started to get displaced. However, since the remaining displacement distance was shorter, only partial displacement was achieved.

When looking closely at the displacement efficiency of 0.97 μm particles at the higher flow rates in the 15 μm devices a lower efficiency was achieved compared to the 30 μm devices, even though the critical diameter of the 15 μm device was lower (Fig. 3 and Table 4). Dincau et al. 2018 showed that the formation of vortices at higher Reynolds numbers (*Re*) could increase the apparent pillar size and hence reduce the resulting pillar gap. To evaluate whether this effect may have contributed in our devices, the Reynolds numbers for the different device parameters and operation modes were estimated (McGrath et al. 2014):

$$Re = \rho \vartheta D_h / \eta \tag{4}$$

with

$$D_h = 2 \underbrace{GH}_{A} / (G + H) \tag{5}$$

The calculated values are shown in Table 5. For the density ρ and viscosity η of water values of $1 \cdot 10^3$ kg/m^3 and $1 \cdot 10^{-3}$ kg/m•s were used, respectively. The hydrodynamic diameter D_h of the channels was calculated with device heights H and pillar gaps G at the respective flow rate (Table 4). The fluid velocity ϑ was estimated by the applied collective flow rate Q_{col} (Table 5) divided by the pillar gap

Table 4 Overview of pillar gap G and critical diameter D_c changes due to different operation conditions

Devices	Pillar gap and critical diameter in μm					
	Wetted		Lower flow rate		Higher flow rate	
	G	D_c	G	D_c	G	D_c
15 μm	2.9	0.6	3.3	0.7	4.3	0.9
30 μm	3.5	0.8	3.9	0.8	5.2	1.1

Table 5 Overview of collective flow rate (Q_{col}), hydrodynamic diameter (D_h) and fluid velocity (ϑ) used for the calculation of Reynolds numbers (Re)

H in μm	15		30	
Q_{col} in μl/min	1.375	5.5	5.5	22
D_h in μm	5.4	6.7	6.9	8.9
ϑ in mm/s	5.4	16.7	9.2	27.7
Re	0.03	0.11	0.06	0.25

cross section area A and number of pillar gaps, n of 85, in a pillar row:

$$\vartheta = Q_{col}/(n \cdot A). \tag{6}$$

The resulting Re were 0.03 and 0.11 for the 15 μm device at lower and higher flow rates and 0.06 and 0.25 for the 30 μm device, respectively. While Re for the 30 μm with the higher flow rate was indeed the highest of the calculated Re values, the absolute value was probably too low (below 1) to explain the higher displacement efficiency of the 30 μm devices compared to the 15 μm devices. As in the works by Dincau et al. (2018) and Kottmeier et al. (2019) the effect of Re on the displacement started at values above 1 and increased with increasing values demonstrated at Re of 10 and above.

Further, the displacement characteristics could be influenced by the device height. Higher devices could possibly compensate perturbations better in the flow profile, which can be caused by particles (Beech 2011) between pillars. So, a particles perturbation between pillars influences relatively less of the total volume for higher devices as the volume increases with device height compared to shallower devices. Also, the effect of clogging, as another perturbation (Beech 2011), could be reduced as a clogged particle in a higher device should be less influential as in a shallower device. As the influence of perturbations is reduced, more stable operation conditions, benefiting the device's separation characteristics, are encountered. In the end, increased height leading to more stable operation conditions may contribute to the increased displacement of 0.97 μm particles in the 30 μm devices.

4 Conclusion

This work investigated the influence of flow rates, and associated with it, total throughputs on the displacement efficiency of PDMS-based DLD devices for sub-micrometer particle separation. For this purpose, devices with different heights exceeding the typical vertical dimensions of

PDMS-based devices (Zeming et al. 2018; Tottori et al. 2020) were manufactured and operated at different flow rates.

By increasing the height of the DLD device a significant increase in throughput, while keeping excellent separation, was achieved. For 0.97 μm particles displacement efficiencies of 97 and 99% for devices with heights of 15 and 30 μm were obtained, even though the flow rate for the 30 μm devices was increased by a factor of four to 0.5 μl/min compared to devices with a height of 15 μm operated at 0.125 μl/min.

Tottori et al. 2020 reported a PDMS-based DLD device for the separation of 0.5 μm and 1.0 μm particles operating at a flow rate of 0.05 μl/min. In comparison, for our device with a height of 30 μm a ten-fold increased flow rate was achieved.

At even further increased flow rates of 0.5 μl/min and 2.0 μl/min for devices with a height of 15 μm and 30 μm, respectively, a reduction in displacement efficiency was seen and investigated. The reduction in displacement efficiency was mainly attributed to flow-rate-induced pillar deformation. This deformation led to larger pillar gaps and hence an increased critical diameter of the devices. Noteworthy, the 30 μm devices showed a smaller reduction in displacement efficiency compared to the 15 μm devices, showing that the increased device height of 30 μm also led to more stable operation conditions.

So, our study showed that increasing the device height enables the separation of sub-μm particles at higher throughputs. Further throughput increases building on these findings can be readily envisioned by combining higher device structure with asymmetric pillar arrays (Zeming et al. 2016), parallelization of devices (Hochstetter et al. 2020; Tottori and Nisisako 2018) or their combinations.

Declarations

Conflict of interest The authors declare that they have no conflicts of interest.

References

Abate AR, Weitz DA (2009) High-order multiple emulsions formed in poly(dimethylsiloxane) microfluidics. Small 5:2030–2032. https://doi.org/10.1002/smll.200900569

Amstad E (2017) Microfluidics: a tool to control the size and composition of particles. Chimia 71:334–341. https://doi.org/10.2533/chimia.2017.334

Azizipour N, Avazpour R, Rosenzweig DH, Sawan M, Ajji A (2020) Evolution of biochip technology: a review from lab-on-a-chip to organ-on-a-chip. Micromachines 11:599. https://doi.org/10.3390/mi11060599

Beech J (2011) Microfluidics separation and analysis of biological particles, PhD Thesis, Lund University, Fasta Tillståndets Fysik. https://portal.research.lu.se/en/publications/microfluidics-separation-and-analysis-of-biological-particles

Campo Ad, Greiner C (2007) SU-8: a photoresist for high-aspect-ratio and 3D submicron lithography. J Micromech Microeng 17:R81–R95. https://doi.org/10.1088/0960-1317/17/6/R01

Datta SS, Abbaspourrad A, Amstad E, Fan J, Kim S-H, Romanowsky M, Shum HC, Sun B, Utada AS, Windbergs M, Zhou S, Weitz DA (2014) 25th anniversary article: double emulsion templated solid microcapsules: mechanics and controlled release. Adv Mater 26:2205–2218. https://doi.org/10.1002/adma.201305119

Davis J (2008) Microfluidic separation of blood components through deterministic lateral displacement. PhD Thesis, Princeton University, Department of Electrical Engineering. https://scholar.princeton.edu/sites/default/files/sturm/files/davis-thesis.pdf

Dincau BM, Aghilinejad A, Hammersley T, Chen X, Kim J-H (2018) Deterministic lateral displacement (DLD) in the high Reynolds number regime: high-throughput and dynamic separation characteristics. Microfluid Nanofluid 22:869. https://doi.org/10.1007/s10404-018-2078-9

Gupta S, Ramesh K, Ahmed S, Kakkar V (2016) Lab-on-chip technology: a review on design trends and future scope in biomedical applications. IJBSBT 8:311–322. https://doi.org/10.14257/ijbsbt.2016.8.5.28

Hochstetter A, Vernekar R, Austin RH, Becker H, Beech JP, Fedosov DA, Gompper G, Kim S-C, Smith JT, Stolovitzky G, Tegenfeldt JO, Wunsch BH, Zeming KK, Krüger T, Inglis DW (2020) Deterministic lateral displacement: challenges and perspectives. ACS Nano 14:10784–10795. https://doi.org/10.1021/acsnano.0c05186

Huang LR, Cox EC, Austin RH, Sturm JC (2004) Continuous particle separation through deterministic lateral displacement. Science 304:987–990. https://doi.org/10.1126/science.1094567

Inglis DW (2009) Efficient microfluidic particle separation arrays. Appl Phys Lett 94:13510. https://doi.org/10.1063/1.3068750

Inglis DW (2010) A method for reducing pressure-induced deformation in silicone microfluidics. Biomicrofluidics. https://doi.org/10.1063/1.3431715

Inglis DW, Morton KJ, Davis JA, Zieziulewicz TJ, Lawrence DA, Austin RH, Sturm JC (2008) Microfluidic device for label-free measurement of platelet activation. Lab Chip 8:925–931. https://doi.org/10.1039/b800721g

Inglis DW, Lord M, Nordon RE (2011) Scaling deterministic lateral displacement arrays for high throughput and dilution-free enrichment of leukocytes. J Micromech Microeng 21:54024. https://doi.org/10.1088/0960-1317/21/5/054024

Jiang J, Zhao H, Shu W, Tian J, Huang Y, Song Y, Wang R, Li E, Slamon D, Hou D, Du X, Zhang L, Chen Y, Wang Q (2017) An integrated microfluidic device for rapid and high-sensitivity analysis of circulating tumor cells. Sci Rep 7:42612. https://doi.org/10.1038/srep42612

Joensson HN, Uhlén M, Svahn HA (2011) Droplet size based separation by deterministic lateral displacement-separating droplets by cell–induced shrinking. Lab Chip 11:1305–1310. https://doi.org/10.1039/c0lc00688b

Kessler M, Elettro H, Heimgartner I, Madasu S, Brakke KA, Gallaire F, Amstad E (2020) Everything in its right place: controlling the local composition of hydrogels using microfluidic traps. Lab Chip 20:4572–4581. https://doi.org/10.1039/d0lc00691b

Kottmeier J, Wullenweber M, Blahout S, Hussong J, Kampen I, Kwade A, Dietzel A (2019) Accelerated particle separation in a DLD device at Re 1 investigated by means of µPIV. Micromachines. https://doi.org/10.3390/mi10110768

Liu Z, Huang F, Du J, Shu W, Feng H, Xu X, Chen Y (2013) Rapid isolation of cancer cells using microfluidic deterministic lateral displacement structure. Biomicrofluidics 7:11801. https://doi.org/10.1063/1.4774308

McGrath J, Jimenez M, Bridle H (2014) Deterministic lateral displacement for particle separation: a review. Lab Chip 14:4139–4158. https://doi.org/10.1039/c4lc00939h

Pariset E, Pudda C, Boizot F, Verplanck N, Berthier J, Thuaire A, Agache V (2017) Anticipating cutoff diameters in deterministic lateral displacement (DLD) microfluidic devices for an optimized particle separation. Small. https://doi.org/10.1002/smll.201701901

Perrotton J, Ahijado-Guzmán R, Moleiro LH, Tinao B, Guerrero-Martinez A, Amstad E, Monroy F, Arriaga LR (2019) Microfluidic fabrication of vesicles with hybrid lipid/nanoparticle bilayer membranes. Soft Matter 15:1388–1395. https://doi.org/10.1039/c8sm02050g

Raj MK, Chakraborty S (2020) PDMS microfluidics: a mini review. J Appl Polym Sci 137:48958. https://doi.org/10.1002/app.48958

Salafi T, Zhang Y, Zhang Y (2019) A review on deterministic lateral displacement for particle separation and detection. Nanomicro Lett 11:77. https://doi.org/10.1007/s40820-019-0308-7

Schindelin J, Arganda-Carreras I, Frise E, Kaynig V, Longair M, Pietzsch T, Preibisch S, Rueden C, Saalfeld S, Schmid B, Tinevez J-Y, White DJ, Hartenstein V, Eliceiri K, Tomancak P, Cardona A (2012) Fiji: an open-source platform for biological-image analysis. Nat Methods 9:676–682. https://doi.org/10.1038/nmeth.2019

Shastri A, McGregor LM, Liu Y, Harris V, Nan H, Mujica M, Vasquez Y, Bhattacharya A, Ma Y, Aizenberg M, Kuksenok O, Balazs AC, Aizenberg J, He X (2015) An aptamer-functionalized chemomechanically modulated biomolecule catch-and-release system. Nat Chem 7:447–454. https://doi.org/10.1038/nchem.2203

Sia SK, Whitesides GM (2003) Microfluidic devices fabricated in poly(dimethylsiloxane) for biological studies. Electrophoresis 24:3563–3576. https://doi.org/10.1002/elps.200305584

Tottori N, Nisisako T (2018) High-throughput production of satellite-free droplets through a parallelized microfluidic deterministic lateral displacement device. Sens Actuators, B Chem 260:918–926. https://doi.org/10.1016/j.snb.2018.01.112

Tottori N, Hatsuzawa T, Nisisako T (2017) Separation of main and satellite droplets in a deterministic lateral displacement microfluidic device. RSC Adv 7:35516–35524. https://doi.org/10.1039/C7RA05852G

Tottori N, Muramoto Y, Sakai H, Nisisako T (2020) Nanoparticle separation through deterministic lateral displacement arrays in poly(dimethylsiloxane). J Chem Eng Japan / JCEJ 53:414–421. https://doi.org/10.1252/jcej.19we160

Velve-Casquillas G, Le Berre M, Piel M, Tran PT (2010) Microfluidic tools for cell biological research. Nano Today 5:28–47. https://doi.org/10.1016/j.nantod.2009.12.001

Vogel N, Utech S, England GT, Shirman T, Phillips KR, Koay N, Burgess IB, Kolle M, Weitz DA, Aizenberg J (2015) Color from hierarchy: diverse optical properties of micron-sized spherical colloidal assemblies. Proc Natl Acad Sci U S A 112:10845–10850. https://doi.org/10.1073/pnas.1506272112

Wang J, Mbah CF, Przybilla T, Apeleo Zubiri B, Spiecker E, Engel M, Vogel N (2018) Magic number colloidal clusters as minimum free energy structures. Nat Commun 9:5259. https://doi.org/10.1038/s41467-018-07600-4

Whitesides GM (2006) The origins and the future of microfluidics. Nature 442:368–373. https://doi.org/10.1038/nature05058

Wunsch BH, Smith JT, Gifford SM, Wang C, Brink M, Bruce RL, Austin RH, Stolovitzky G, Astier Y (2016) Nanoscale lateral displacement arrays for the separation of exosomes and colloids down to 20 nm. Nat Nanotechnol 11:936–940. https://doi.org/10.1038/nnano.2016.134

Zeming KK, Salafi T, Chen C-H, Zhang Y (2016) Asymmetrical deterministic lateral displacement gaps for dual functions of enhanced separation and throughput of red blood cells. Sci Rep 6:22934. https://doi.org/10.1038/srep22934

Zeming KK, Salafi T, Shikha S, Zhang Y (2018) Fluorescent label-free quantitative detection of nano-sized bioparticles using a pillar array. Nat Commun 9:1254. https://doi.org/10.1038/s41467-018-03596-z

Zhang Y, Lo C-W, Taylor JA, Yang S (2006) Replica molding of high-aspect-ratio polymeric nanopillar arrays with high fidelity. Langmuir 22:8595–8601. https://doi.org/10.1021/la061372+

Zhang B, Korolj A, Lai BFL, Radisic M (2018) Advances in organ-on-a-chip engineering. Nat Rev Mater 3:257–278. https://doi.org/10.1038/s41578-018-0034-7